

Dynamical mass of the white dwarf in XY Ari: a test for intermediate polar X-ray spectral models

A. Álvarez-Hernández^{1,2*}, M. A. P. Torres^{1,2}, P. Rodríguez-Gil^{1,2}, T. Shahbaz^{1,2}, J. Sánchez-Sierras^{1,2}, J. A. Acosta-Pulido^{1,2}, P. G. Jonker^{3,4}, K. D. Gazeas⁵, P. Hakala⁶, J. M. Corral-Santana⁷

¹*Instituto de Astrofísica de Canarias, E-38205 La Laguna, Tenerife, Spain*

²*Departamento de Astrofísica, Universidad de La Laguna, E-38206 La Laguna, Tenerife, Spain*

³*SRON, Netherlands Institute for Space Research, Niels Bohrweg 4, 2333 CA, Leiden, The Netherlands*

⁴*Department of Astrophysics/ IMAPP, Radboud University, Heyendaalseweg 135, 6525 AJ, Nijmegen, The Netherlands*

⁵*Section of Astrophysics, Astronomy and Mechanics, Department of Physics, National and Kapodistrian University of Athens, GR-15784 Zografos, Athens, Greece*

⁶*Finnish Centre for Astronomy with ESO (FINCA), Quantum, Vesilinnantie 5, FI-20014 University of Turku, Finland*

⁷*European Southern Observatory, Alonso de Córdova 3107, Vitacura, Casilla 19001, Santiago de Chile, Chile*

Accepted XXX. Received YYY; in original form ZZZ

ABSTRACT

We present a dynamical study of the eclipsing intermediate polar XY Ari based on time-resolved near-infrared spectroscopy obtained with the EMIR spectrograph on the 10.4-m Gran Telescopio Canarias. Using main sequence template spectra taken with the same instrument setup as the target spectra, we measure a radial velocity amplitude of the late K-type donor star $K_2 = 256 \pm 2 \text{ km s}^{-1}$. We also obtain the rotational broadening of its photospheric lines $v_{\text{rot}} \sin i = 141 \pm 3 \text{ km s}^{-1}$. From these and the eclipse geometry, we derive a donor-to-white-dwarf mass ratio $q = M_2/M_1 = 0.62 \pm 0.02$, an orbital inclination $i = 80.8^\circ \pm 0.5^\circ$ and dynamical masses $M_1 = 1.21 \pm 0.04 M_\odot$ and $M_2 = 0.75 \pm 0.04 M_\odot$ (1σ). This result places the white dwarf in XY Ari as one of the three most massive known in a cataclysmic variable. Comparison with white dwarf mass estimates from X-ray spectral studies could indicate the necessity of an improvement of the X-ray models and/or analysis techniques, as a number of X-ray white dwarf masses are in disagreement with the dynamical mass value.

Key words: accretion, accretion discs – binaries: close – novae, cataclysmic variables – stars: individual: XY Ari

1 INTRODUCTION

Cataclysmic variables (CVs) are binary systems typically consisting of a non-degenerate donor star that fills its Roche lobe and transfers mass to a white dwarf (WD) primary star (Kraft 1964, see Warner 1995 for a review). In the subclass of CVs known as intermediate polars (IPs), the WD has a relatively intense magnetic field ($10^4 - 10^6 \text{ G}$), which is not strong enough to disrupt the accretion disc entirely (as in the case of the polar CVs). Instead, the disc is truncated at some radius from the WD and the accretion flow is conducted from there to the WD magnetic poles following the field lines.

XY Ari is an IP first discovered by the *Einstein* satellite as an X-ray source (1H 0253+193) coincident with the centre of the molecular cloud Lynds 1457 (Halpern & Patterson 1987). For this reason, it was initially suggested as a T Tauri star embedded in the cloud. Observations performed with the *Ginga* satellite discovered coherent pulsations with a period of $\approx 206 \text{ s}$ (Takano et al. 1989; Koyama et al. 1991). Based on this, Patterson & Halpern (1990) rejected the possibility of 1H 0253+193 being an X-ray binary and proposed either an isolated WD or neutron star accreting gas from the cloud or a CV. Later, Kamata et al. (1991) discovered periodic dips in

the X-ray light curve with a period of $21829 \text{ s} \approx 6.06 \text{ h}$, which were interpreted as eclipses of the X-ray source produced by the transit of a donor star. They concluded that 1H 0253+193 is most likely a CV located behind Lynds 1457. Zuckerman et al. (1992) identified the near-infrared (NIR) counterpart at $J \approx 16.0$, $H \approx 14.2$ and $K \approx 13.3$. Similar magnitudes were reported in the Two Micron All Sky Survey (2MASS; Cutri et al. 2003). All these values correspond to the quiescent state of the system, since XY Ari is known to undergo dwarf nova outbursts (Hellier et al. 1997). Due to the high extinction produced by the molecular cloud, XY Ari is only fully detected in the redder bandpasses of the Sloan Digital Sky Survey (SDSS) and Panoramic Survey Telescope and Rapid Response System (Pan-STARRS) surveys at $i = 22 - 21.5$, $z = 20.0 - 19.4$ (Alam et al. 2015; Chambers et al. 2016).

Some of the orbital parameters of XY Ari have been robustly measured from X-ray and NIR data. Allan et al. (1996) took H -band photometry covering more than three orbits of the system. Combining eclipse timings from their light curves and from Kamata et al. (1991) and Zuckerman et al. (1992), they derived precise mid-eclipse ephemeris. They also modelled their H -band light curve, which is dominated by the ellipsoidal variation caused by the change of the projected surface of a non-irradiated Roche-lobe-filling donor star with orbital phase. From the modelling they set constraints of

* E-mail: ayozeav@iac.es

Table 1. Log of the XY Ari GTC/EMIR spectroscopy. Orbital phases are calculated using the ephemeris derived in Section 3.1. The on-source time was 480 s for each ABBA cycle. The seeing values correspond to the FWHM of the spatial profile at spectral positions near $\lambda = 2.2 \mu\text{m}$. Magnitudes for XY Ari were measured in the acquisition images by performing differential photometry relative to the nearby star 2MASS 02561213+1925362.

Date	ABBA cycles	Orbital phase coverage	Airmass	Seeing (arcsec)	K_s (mag)
2018 Dec 27	4	0.63–0.71	1.18–1.26	0.7–0.9	13.5–14.0
2020 Jan 05	4	0.15–0.23	1.01–1.02	0.9–1.0	13.1–13.2
2020 Sep 28	4	0.68–0.75	1.02–1.05	0.9–1.1	13.5
2020 Sep 30	8	0.92–0.99, 0.12–0.20	1.04–1.22	0.7–0.8	13.2–13.9
2020 Oct 01	8	0.79–0.86, 0.98–0.06	1.01–1.14	0.6–0.7	13.4–13.9
2020 Nov 23	8	0.25–0.32, 0.49–0.56	1.09–1.50	1.0–0.8	13.2–13.5
2022 Feb 11	4	0.50–0.57	1.48–1.67	1.0–1.3	*

* Acquisition in the J -band. We measure $J = 16.1 - 16.6$.

$0.43 < q < 0.71$ and $80^\circ < i < 87^\circ$ on the binary mass ratio and the orbital inclination, respectively. Hellier (1997) used X-ray data from the *RXTE* satellite to study the accreting regions of the WD and found that accretion takes place on both magnetic poles, which can be seen in quiescence. From imposing that the lower accreting pole of the WD is seen through the inner hole in the accretion disc, he refined the previous ranges to $0.48 < q < 0.68$ and $80^\circ < i < 84^\circ$. Later, Littlefair et al. (2001) presented low-resolution K -band spectroscopy and applied the optimal subtraction technique (Marsh et al. 1994) to classify the donor star. Their results supported a $K7 - M0$ V spectral type, most probable $M0 \pm 0.5$ V.

Dynamical masses of the stellar components in XY Ari have never been derived, since the radial velocity amplitude of the donor star has not been measured and the binary mass ratio is poorly constrained. Estimates of the WD mass from X-ray spectral modelling have been reported, but the results are highly inconsistent with each other, with masses in a wide range ($0.80 - 1.50 M_\odot$ at 1σ). In this work, we present a complete dynamical study of XY Ari, obtaining for the first time robust values of the stellar masses. We compare our results with previous estimates from X-ray spectroscopy and provide valuable feedback to the X-ray spectral modelling.

The article is structured as follows: in Section 2 we present our K -band spectroscopic observations and their reduction. From their analysis we obtain the radial velocity curve of the donor star (Section 3.1), its spectral type (Section 3.2) and rotational broadening of the absorption lines (Section 3.3). We then derive the binary mass ratio, the orbital inclination and the dynamical masses (Section 3.4). In Section 4 we discuss our results and in Section 5 we present our conclusions.

2 OBSERVATIONS AND DATA REDUCTION

We obtained NIR spectroscopy of XY Ari using the EMIR spectrograph (Garzón & EMIR Team 2016; Garzón et al. 2022) attached to the 10.4-m Gran Telescopio Canarias at the Observatorio del Roque de los Muchachos on the island of La Palma, Spain. The target was observed in queue mode at different epochs between 2018 – 2022, covering $\simeq 65$ per cent of its 6.06-h orbit. We used the K -grism and implemented with the Configurable Slit Unit a 0.6-arcsec wide long slit positioned one arcmin left from the centre of the field of view. This instrument setup covered the $2.08 - 2.43 \mu\text{m}$ wavelength range with a dispersion of $1.71 \text{ \AA pix}^{-1}$ and a resolution of $\simeq 4.8 \text{ \AA}$ full-width at half-maximum (FWHM), as measured from the atmospheric OH emission lines. This is equivalent to $\simeq 65 \text{ km s}^{-1}$ at

$2.2 \mu\text{m}$. Each observing visit (block) to the target consisted of four consecutive ABBA nodding cycles using a nod of 12 arcsec and 120-s individual exposures. In total, we obtained 40 ABBA cycles on seven different nights (see Table 1 for a log of the observations). Only the last night data were taken at an airmass larger than 1.5.

We also took spectra of template stars with the same setup as for XY Ari. We observed main sequence stars with effective temperatures in the range 3020 – 4500 K, covering spectral types from K4 to M5, selected from the samples in Rojas-Ayala et al. (2012) and Yee et al. (2017). All these template stars have low rotational velocities. For telluric line removal, we took spectra of A0 V stars close in sky position and time to the science and template spectra. The image quality measured by fitting the spatial profiles of the XY Ari, template and telluric star spectra showed that all data were taken under slit-limited conditions (see Table 1).

The data reduction was performed using version 0.17.0 of the PYEMIR package (Cardiel et al. 2019). After dark and flat-field correction, the wavelength calibration and rectification were performed over the 2D frames using the sky OH emission lines. The rms scatter of the fits was $0.5 - 0.8 \text{ \AA}$ (equivalent to $7 - 11 \text{ km s}^{-1}$) for all data sets. The wavelength calibration was examined by checking the telluric absorption features in the XY Ari data relative to their average spectrum, finding minor shifts with a standard deviation of 5 km s^{-1} . The four spectra of each ABBA cycle were averaged, sky subtracted and dithering corrected to obtain one spectrum per nodding cycle. This spectrum was extracted with the *apall* task in IRAF¹.

Two different techniques for the removal of telluric absorption features were tested. The first technique derives the Earth’s atmospheric transmission by modelling the intrinsic spectra of the A0 V stars that were obtained close to each XY Ari observation. This was done with a modified version of the XTLLCOR GENERAL (IDL) package (Vacca et al. 2003). The second technique computes the atmospheric transmission spectrum from fitting the telluric absorptions in the science spectra. These fits were computed using version 1.5.9 of MOLECFIT (Smette et al. 2015). For this method, the EMIR data format was adapted to MOLECFIT using custom PYTHON 3.7 routines, and we masked out from the fit regions with spectral features prominent in K- and M-type stars. We found agreement between the two methods at the 1σ level for all the parameters measured in this work. In the paper, we present the results obtained with the MOLECFIT correction, avoiding in this way the use of some low signal-to-noise ratio (SNR) A0 V spectra.

¹ IRAF is distributed by the National Optical Astronomy Observatories.

To perform the analysis described in the next sections we imported the telluric-corrected spectra into MOLLY². We corrected for the Earth motion and shifted the spectra to the heliocentric rest frame. The spectra were normalised to a spline-fitted continuum and rebinned into a logarithmic scale which provides an uniform velocity scale. The mid-exposure times for each spectrum were calculated and expressed in heliocentric Julian days (UTC). This was also done for the high SNR (≥ 80) library spectra presented in Section 3.2. We used them for the spectral classification of the donor star because not all of the observed templates have enough SNR for this task.

3 ANALYSIS AND RESULTS

The measurements in this section were obtained in the wavelength ranges 2.09 – 2.15 and 2.18 – 2.27 μm unless otherwise stated. We did not use the molecular bands at wavelengths $> 2.27 \mu\text{m}$ due to a much lower SNR. All uncertainties presented in this paper are quoted at 68 per cent confidence level. Finally, the spectral types assigned to the templates are based on the effective temperature - spectral class correspondence in Pecaut & Mamajek (2013).

3.1 Radial velocity curve of the donor star

We measured the radial velocities by cross-correlating each XY Ari spectrum with either the HIP 40375, HIP 40910, HD 157881 or HD 232979 observed templates, that match the spectral type range of the donor star in XY Ari (more details in Sections 3.2 and 3.3). Previous to cross-correlation, the template spectra were corrected for their radial velocities³, broadened to match the projected rotational velocity ($v_{\text{rot}} \sin i$) of the donor star (measured in Section 3.3) and rebinned onto the same logarithm scale as the XY Ari spectra. We added quadratically the 5 km s^{-1} uncertainty in the wavelength calibration (Section 2) to the statistical error of each radial velocity measurement. We performed least-squares sinusoidal fits to the radial velocity curves of XY Ari, $V(t)$, of the form:

$$V(t) = \gamma + K_2 \sin \left[\frac{2\pi}{P} (t - T_0) \right], \quad (1)$$

where γ is the heliocentric systemic velocity, K_2 the radial velocity amplitude of the donor star, P the orbital period and T_0 the time of closest approach of the donor star to the observer. The orbital period is determined at $P = 0.25269664(6)$ d from eclipse timing in X-ray and NIR data taken between 1989 and 1995 (Allan et al. 1996). Hence, we fixed it in the fits. In Table 2 we present the best-fit parameters. Note that excluding from the fits the low SNR data from 2022 February does not change the resulting parameters. There are no significant differences between the results using different templates, and the χ^2 of the fits is 37 – 41 for 37 degrees of freedom (dof). Hence, we adopt the mean for all the parameters, taking the conservative approach of maintaining the statistical uncertainty from the individual values instead of the standard deviation. Our average values are $\gamma = 22 \pm 5 \text{ km s}^{-1}$, $K_2 = 256 \pm 2 \text{ km s}^{-1}$ and T_0 (HJD) = 2459122.7116 \pm

² <http://deneb.astro.warwick.ac.uk/phsaap/software/molly/html/INDEX.html>

³ HIP 40375 and HD 157881 have *Gaia* radial velocities of $21.393 \pm 0.002 \text{ km s}^{-1}$ and $-23.523 \pm 0.002 \text{ km s}^{-1}$, respectively (Soubiran et al. 2018). According to Chubak & Marcy (2011), HIP 40910 has a radial velocity of $7.0 \pm 0.2 \text{ km s}^{-1}$. From Fouqué et al. (2018), HD 232979 has a radial velocity of $34.2 \pm 0.3 \text{ km s}^{-1}$.

Table 2. Donor star radial velocity curve best-fit parameters. The numbers in brackets indicate the uncertainty on the last digit. The 5 km s^{-1} uncertainty in the wavelength calibration was quadratically added to the uncertainties of the γ values. Degrees of freedom (dof) = 37.

Template	γ (km s^{-1})	K_2 (km s^{-1})	T_0 (HJD)	χ^2/dof
HIP 40375	20(5)	257(2)	2459122.7117(5)	1.03
HIP 40910	25(5)	256(2)	2459122.7114(5)	0.99
HD 157881	25(5)	257(2)	2459122.7117(4)	1.11
HD 232979	16(5)	256(2)	2459122.7115(5)	1.08

0.0005. Fig. 1 shows the phase-folded radial velocity curve obtained with the HIP 40910 template together with the best-fit sine wave.

Irradiation of the donor star by the WD may affect the K_2 measurement by shifting the light centre of the absorption lines (Hessman et al. 1984; Marsh 1988; Wade & Horne 1988). To check if this is the case in XY Ari, we fitted our radial velocity curves using an elliptical orbit. Following Martin et al. (1987), we used the Wilsing-Russell method (see Luyten 1936) suitable for eccentricities $e \leq 0.1$. We find $e = 0.004 \pm 0.012$, which is compatible with null eccentricity and is significantly lower than what is found for CVs with irradiated donor stars like AM Her ($e = 0.05 - 0.07$, Southwell et al. 1995), IP Peg ($e = 0.089 \pm 0.020$, Martin et al. 1989) or DO Dra/YY Dra ($e = 0.056 \pm 0.026$, Mateo et al. 1991). We also fitted a circular orbit to the radial velocities in the orbital phase range 0.8 – 1.2, when we see the side of the donor that is not facing the WD. This allows to derive K_2 when the donor star is irradiated (Davey & Smith 1992; Billington et al. 1996). We obtained $K_2 = 261 \pm 4 \text{ km s}^{-1}$, which agrees at the 1σ level with the value obtained by fitting the whole orbit. Based on these two tests, we conclude that our radial velocity curve is unlikely to be affected by heating.

When examining the implications of our T_0 value, we found a phase shift of ≈ 0.11 cycle relative to the orbital phases predicted by the linear ephemeris of Allan et al. (1996) for our data. In this regard, Hellier (1997) found an accumulated shift of 0.0077 when applying the ephemeris to *RXTE* data obtained in 1996, while Zengin Camurdan et al. (2018) reported a 0.067 mid-eclipse phase shift when phase-folding *XMM-Newton* data taken in 2010. The uncertainty in the orbital period given by Allan et al. (1996) amounts to an accumulated error of ≈ 0.013 cycle after 44998 orbits between their T_0 and ours. Possible explanations for this discrepancy are changes in the orbital period over time or an underestimate of the uncertainty due to unaccounted for systematics in Allan et al.’s eclipse time measurements. For instance, the presence of flickering in their NIR light curves could have skewed some of the mid-eclipse time determinations. In addition, their mid-ingress/egress time measurements from X-ray data could be affected by inaccuracies due to not having enough time resolution (see e.g. figure 3 in Kamata et al. 1991) and/or changes in the relative position of the two X-ray emitting poles between eclipses due to the WD rotation (Hellier 1997). To obtain an accumulated error that matches the observed phase shift, the uncertainty in the orbital period should be ≈ 10 times higher than reported by Allan et al. (1996), i.e. $10 \times (6 \times 10^{-8} \text{ d}) \approx 0.05 \text{ s}$.

3.2 Spectral classification of the donor star

In order to constrain the spectral type of the donor star in XY Ari we used two grids of high SNR public spectra of K- and M-type stars. The first grid contains thirteen templates with $R = \lambda/\Delta\lambda \approx 2000$

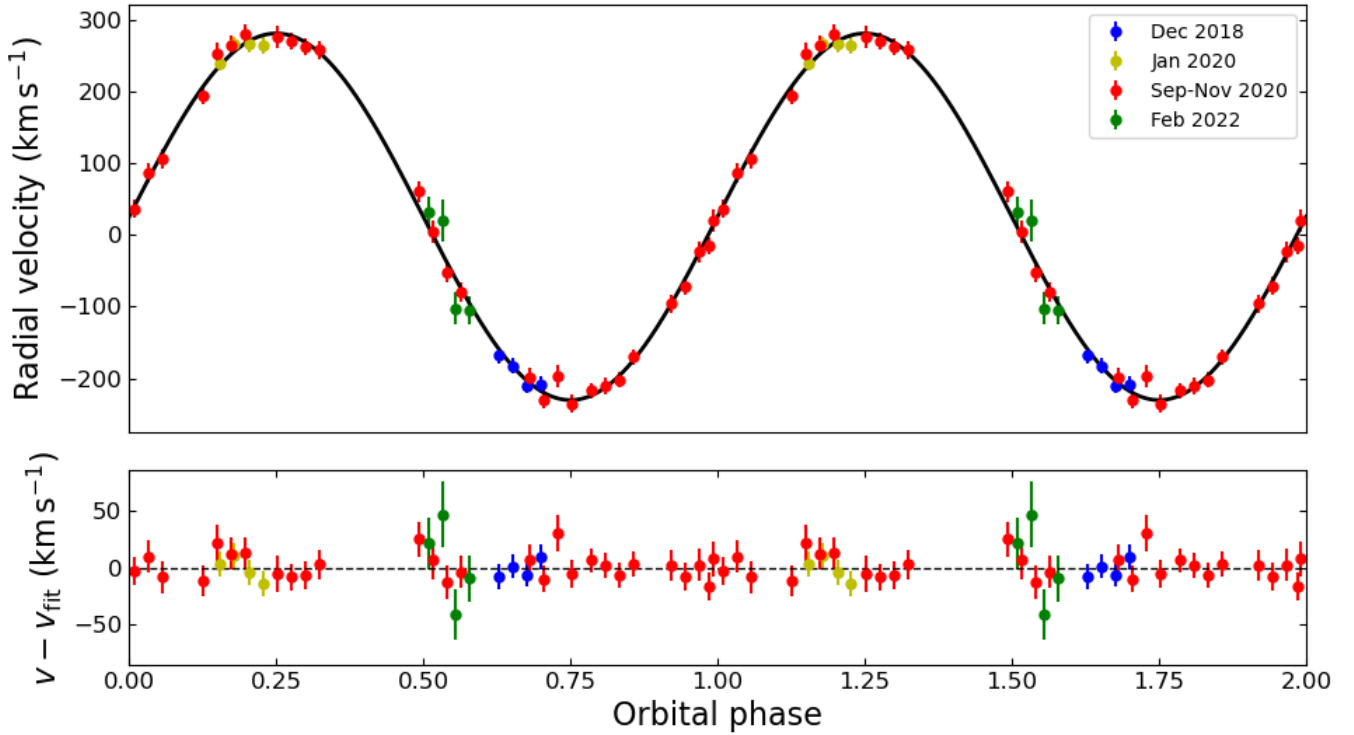


Figure 1. Top panel: Phase-folded heliocentric radial velocity curve of the donor star in XY Ari obtained by cross-correlating the individual spectra with the template spectrum HIP 40910. The best sinusoidal fit is shown as a black line and the orbital cycle has been repeated for the sake of clarity. Bottom panel: residuals of the fit.

covering $0.8 - 2.5 \mu\text{m}$ and extracted from the InfraRed Telescope Facility (IRTF) spectral library (Rayner et al. 2009). For K-type dwarfs we took the average photometric effective temperature estimates provided in Luck (2017), while for M-dwarfs we used the photometric effective temperatures given in Houdebine et al. (2019). This was not possible for two objects (HD 45977 and HD 237903), for which we adopted the temperature values from Sousa et al. (2011) and Niedzielski et al. (2016), respectively. The resolution of this grid is comparable to the broadening of the XY Ari data resulting from convolution of the instrumental and the rotational profiles. The second grid includes eight high resolution ($R = \lambda/\Delta\lambda \approx 10000$) spectra from the X-shooter Spectral Library (XSL) Data Release 2 (Gonneau et al. 2020). The effective temperatures were spectroscopically derived by Arentsen et al. (2019). From visual inspection, we selected the XSL spectra less affected by emission spike artifacts in the wavelength regions used in our analysis. However, all of them suffer from artifacts at $\approx 2.26 - 2.28 \mu\text{m}$ due to imperfect order merging. Thus, we were forced to perform the analysis in the $2.09 - 2.15$ and $2.18 - 2.25 \mu\text{m}$ regions with the caveat that compared to the IRTF templates we do not cover the Ca I photospheric lines. Table 3 lists all the IRTF and XSL selected templates.

We applied the optimal subtraction technique described in Marsh et al. (1994) to all the XY Ari spectra with both grids of templates. It searches for the smoothest residual obtained after subtracting a set of normalized spectral templates from the average, Doppler-corrected and normalized spectrum of the target (see e.g. Fig. 3). In the case of the XSL grid, we previously downgraded the spectral templates to match the resolution of the XY Ari spectra by convolution with a Gaussian profile with $\text{FWHM} = 63 \text{ km s}^{-1}$. We summarize here how we applied the optimal subtraction technique with each of the

templates. First, we velocity-shifted each XY Ari spectrum to the rest frame of the template. Next, we computed a weighted average of the XY Ari spectra giving larger weights to those with higher SNR. We subsequently broadened the photospheric lines of the template spectrum by convolution with the Gray’s rotational profile (Gray 1992). We adopt a linear limb-darkening coefficient for the K -band of 0.25, a reasonable choice for a late K-type star (Claret et al. 1995) and probed the $v_{\text{rot}} \sin i$ space between 1 and 200 km s^{-1} in steps of 1 km s^{-1} . A robust measurement of $v_{\text{rot}} \sin i$ will be given in Section 3.3, where we will use templates taken with the same instrumental setup as the XY Ari data. The broadened versions of each template were multiplied by a factor f between 0 and 1 and then subtracted from the weighted-average spectrum of XY Ari. This factor represents the fractional contribution of the donor star to the total flux in the wavelength range of the analysis. Finally, we searched for the values of $v_{\text{rot}} \sin i$ and f that minimised the χ^2 between the residual of the subtraction and a smoothed version of itself obtained by convolution with a Gaussian profile with $\text{FWHM} = 30 \text{ \AA}$. This smoothing removes large-scale trends in the residual spectrum.

The top panel in Fig. 2 shows the minimum χ^2/dof for each template. The minimization of χ^2/dof shows a plateau in the effective temperature range $3850 - 4250 \text{ K}$. Visual inspection of the broadened versions of the IRTF/XSL templates in that range and the XY Ari average spectrum did not allow to obtain a narrower constraint for the spectral type of the donor. According to Pecaut & Mamajek (2013), the $3850 - 4250 \text{ K}$ effective temperature range corresponds to K6 – M0 V. Littlefair et al. (2001) applied a similar χ^2 -based analysis employing the average of K -band spectra obtained with a $\approx 350 \text{ km s}^{-1}$ resolution that covered orbital phases $0.64 - 0.18$. They found a K7 – M0 V donor star, which agrees with our constraint.

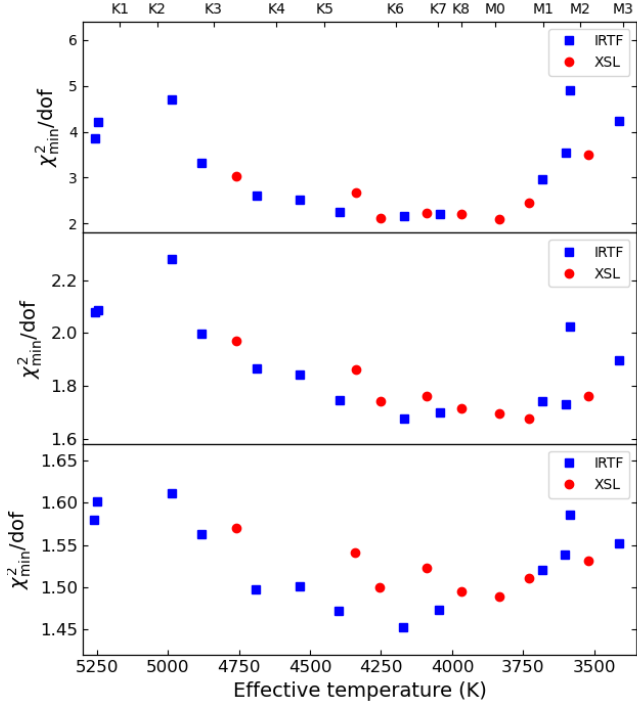


Figure 2. Spectral classification of the donor star using the optimal subtraction technique with template spectra from IRTF (blue squares) and XSL (red circles). Results are shown for the full average spectrum of XY Ari (top panel) and averages at orbital phases 0.9 – 0.1 (middle panel) and 0.4 – 0.6 (bottom panel). The spectral type – effective temperature correspondence is indicated.

We searched for differences in the temperature of the donor’s day and night hemispheres. To do so, we produced average spectra at orbital phases 0.9 – 0.1 (night side, from eight individual spectra) and 0.4 – 0.6 (day side, from eight individual spectra, being four of them those with low SNR taken on 2022 February). We then repeated the optimal subtraction process for both cases. The middle and bottom panels of Fig. 2 show the results for phases 0.9 – 0.1 and 0.4 – 0.6, respectively. Compared to the results of the full average, the χ^2_{\min}/dof –effective temperature relation is less abrupt for the day- and night-side averages as a consequence of the lower SNR. Nevertheless, the IRTF grid template spectra (covering more photospheric lines than the XSL grid) show that the lowest χ^2_{\min}/dof corresponds to the template HD 201092 for both the day- and night-side averages. This template has an effective temperature of 4171 ± 39 K, in line with a K6 V spectral type. We consider this, together with the null eccentricity in the radial velocity curve (Section 3.1), as evidence of no significant heating of the donor star photosphere. Allan et al. (1996) reached the same conclusion based on the study of their *H*-band ellipsoidal+eclipse light curve. As a final test, we also looked for a narrow component in the Br γ emission line, that may originate on the irradiated face of the donor star if heating were significant. For this we inspected the emission-line trailed spectrogram (not shown), but we did not detect any sign of such a feature.

3.3 Projected rotational velocity of the donor star

We exploit again the optimal subtraction technique, this time to measure $v_{\text{rot}} \sin i$ using four of the spectral templates of dwarfs taken with

Table 3. IRTF and XSL templates used for the spectral classification.

Template	Library	Sp. Type	Effective temperature (K)	Ref.
HD 10476	IRTF	K0 V	5259 ± 55	<i>a</i>
HD 145675	IRTF	K0 V	5248 ± 79	<i>a</i>
HD 3765	IRTF	K2.5 V	4987 ± 32	<i>a</i>
HD 219134	IRTF	K3 V	4883 ± 56	<i>a</i>
HD 45977	IRTF	K4 V	4689 ± 174	<i>b</i>
HD 36003	IRTF	K4.5 V	4536 ± 28	<i>a</i>
HD 237903	IRTF	K5 V	4398 ± 32	<i>c</i>
HD 201092	IRTF	K6 V	4171 ± 39	<i>a</i>
HD 19305	IRTF	K7 V	4045 ± 13	<i>d</i>
HD 42581	IRTF	M1 V	3683 ± 13	<i>d</i>
HD 95735	IRTF	M1.5 V	3603 ± 13	<i>d</i>
Gl 806	IRTF	M2 V	3587 ± 13	<i>d</i>
Gl 388	IRTF	M3 V	3414 ± 13	<i>d</i>
HD 218566	XSL	K3.5 V	4761 ± 50	<i>e</i>
HD 21197	XSL	K5.5 V	4340 ± 45	<i>e</i>
HD 118100	XSL	K6 V	4255 ± 44	<i>e</i>
HD 204587	XSL	K7 V	4091 ± 43	<i>e</i>
HIP 70472	XSL	K8 V	3968 ± 52	<i>e</i>
HIP 100047	XSL	M0 V	3835 ± 50	<i>e</i>
HD 209290	XSL	M0.5 V	3731 ± 59	<i>e</i>
HD 119850	XSL	M2 V	3521 ± 56	<i>e</i>

^aLuck (2015)

^bSousa et al. (2011)

^cNiedzielski et al. (2016)

^dHoudebine et al. (2019)

^eArentsen et al. (2019)

Table 4. $v_{\text{rot}} \sin i$ and f from optimal subtraction of the template spectra observed with the same instrumental setup employed for XY Ari. The numbers in brackets indicate the uncertainties on the last digit.

Template	Sp. Type	Effective temperature (K)	$v_{\text{rot}} \sin i$ (km s ⁻¹)	f
HIP 40375	K4–K7 V	4334 ± 209	142(3)	0.78(2)
HIP 40910	K5–K8 V	4159 ± 228	142(3)	0.83(2)
HD 157881	K6–K7 V	4124 ± 60	139(3)	0.65(2)
HD 232979	K8–K9 V	3929 ± 60	141(4)	0.72(2)

EMIR (Section 2). These templates, listed in Table 4, are affected by the same instrumental broadening as the target spectra, making them ideal to properly measure $v_{\text{rot}} \sin i$. The effective temperature of these templates is within the constraint for the donor star of XY Ari found in the previous section.

For the measurement of $v_{\text{rot}} \sin i$ we simulated the effect of the drift in the donor’s absorption lines during the exposures by making one copy of a given template for each science spectrum, smearing them according to the effective length of the science exposures and the orbital parameters, and finally computing an average from those copies (see e.g. Torres et al. 2002).

We compared the results obtained using different FWHM values (between 1 and 50 Å) of the smoothing Gaussian that is applied to the residual during the optimal subtraction process. The impact of the FWHM on $v_{\text{rot}} \sin i$ was < 5 km s⁻¹ with a weak parabolic relationship between the resulting $v_{\text{rot}} \sin i$ and the selected FWHM, with a

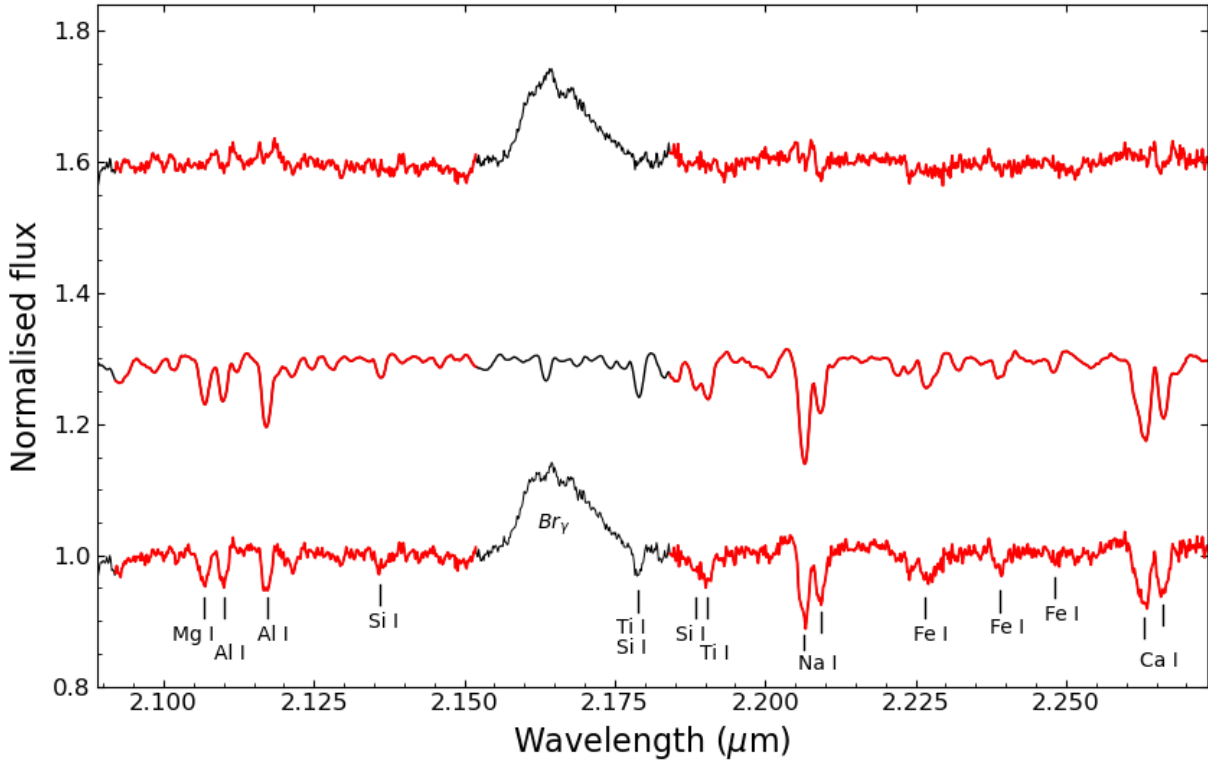


Figure 3. Illustration of the optimal subtraction technique. From bottom to top: XY Ari average spectrum in the rest frame of the donor star, spectrum of the HD 157881 template (K6–K7 V) observed with the same instrument setup and broadened to match the donor star’s $v_{\text{rot}} \sin i$, and the residual after subtraction of the broadened and scaled template. The wavelength regions used for the analysis presented in Sections 3.1, 3.2 (for the IRTF templates) and 3.3 are marked in red. The template and residual spectra have been shifted vertically for display purposes. The main spectral features are identified according to the NASA IRTF spectral library atlas (Rayner et al. 2009).

minimum at $\approx 30 \text{ \AA}$. Performing this analysis with four artificially broadened templates resulted in very similar trends and showed that the minimum $v_{\text{rot}} \sin i$ is the actual broadening applied to the data. Hence, we finally selected the results obtained using a 30- \AA FWHM smoothing Gaussian.

Evaluation of the uncertainties in $v_{\text{rot}} \sin i$ and f was performed by Monte Carlo randomization following the approach in Steeghs & Jonker (2007) and Torres et al. (2020). For each template, the optimal subtraction procedure was repeated for 10000 bootstrapped copies of the XY Ari average spectrum. This delivered normal distributions of possible values for $v_{\text{rot}} \sin i$ and f , so we took their mean and standard deviation as the value and 1σ uncertainty, respectively.

The best $v_{\text{rot}} \sin i$ and f for each template are presented in Table 4. Based on these measurements, we adopt a mean $v_{\text{rot}} \sin i = 141 \pm 3 \text{ km s}^{-1}$, deriving the uncertainty as we did for the parameters presented in Section 3.1. In this case, this conservative approach serves to account for the potential systematic uncertainties induced by the choice of the limb-darkening coefficient. In this regard, using values of 0 and 0.5 changes the $v_{\text{rot}} \sin i$ by -3 and $+3 \text{ km s}^{-1}$, respectively. Our XY Ari spectra do not cover the full orbital cycle, but they have a pretty even sampling of the orbital phases critical to account for the $v_{\text{rot}} \sin i$ variability. Thus, the $v_{\text{rot}} \sin i$ value presented here must serve as a good measure of its mean value around the full orbit. In fact, we arrive at a similar result adopting the mean value of the $v_{\text{rot}} \sin i$ measurements obtained from the spectra observed at the 0.9–0.1, 0.15–0.35, 0.4–0.6 and 0.65–0.85 orbital phase ranges. From the measurements presented in Table 4 we also conclude that

the donor star contributes $\approx 70 - 80$ per cent to the total flux in the K_s -band at the time of our spectroscopy.

3.4 Binary mass ratio, orbital inclination and stellar masses

We derived the donor-to-WD mass ratio ($q = M_2/M_1$) for XY Ari using the equation:

$$v_{\text{rot}} \sin i \approx 0.49(1+q)q^{2/3}K_2 \left[0.6q^{2/3} + \ln(1+q^{1/3}) \right]^{-1}, \quad (2)$$

which is obtained using a spherical approximation for the Roche Lobe radius of the donor star (Eggleton 1983) and making some natural assumptions for the system: circular orbit, synchronized rotation of the donor star with the orbital motion, and alignment of the orbital and stellar spin axes. To compute the uncertainty in q we followed a Monte Carlo approach that picked random values of K_2 and $v_{\text{rot}} \sin i$ from normal distributions defined by the mean and the 1σ uncertainties of our measurements. We then constructed a probability distribution for q by calculating its value for 10000 random sets of K_2 and $v_{\text{rot}} \sin i$. This distribution was well fitted with a Gaussian, so we took its mean and standard deviation as reliable estimates of q and its uncertainty, respectively. We derive below the uncertainties in i , M_1 and M_2 following the same Monte Carlo approach.

Using the values of K_2 and $v_{\text{rot}} \sin i$ derived in Sections 3.1 and 3.3 in Eq. 2, we obtain

$$q = 0.62 \pm 0.02, \quad (3)$$

which is within the $0.48 < q < 0.68$ range proposed by [Hellier \(1997\)](#).

The orbital inclination, i , can be inferred from q and the width of the X-ray eclipse considering when a point is eclipsed by the photosphere of the Roche-lobe-filling donor star. [Chanana et al. \(1976\)](#) set through ray tracing the eclipse limit conditions in their eq. 4 and 5. We solve this system of non-linear equations following the minimization approach described by the authors. Using the derived q , an average mid-ingress to mid-egress eclipse duration of 2050 ± 28 s ([Kamata et al. 1991](#); [Allan et al. 1996](#)) and the Broyden–Fletcher–Goldfarb–Shanno algorithm we obtain:⁴

$$i = 80.8^\circ \pm 0.5^\circ, \quad (4)$$

which agrees with previous constraints of $80^\circ < i < 87^\circ$ ([Allan et al. 1996](#)) and $80^\circ < i < 84^\circ$ ([Hellier 1997](#)).

Finally, from our K_2 , q and i values and the orbital period of [Allan et al. \(1996\)](#), considering a ± 0.05 s uncertainty, we obtain the masses of the stars in XY Ari to be:

$$M_1 = \frac{P(1+q)^2}{2\pi G} \frac{K_2^3}{\sin^3 i} = 1.21 \pm 0.04 M_\odot \quad (5)$$

$$M_2 = qM_1 = 0.75 \pm 0.04 M_\odot. \quad (6)$$

The inclination was derived under the assumption that the source of the X-ray emission eclipsed by the donor star is centred on the WD. This is unlikely, since the WD in XY Ari shows during quiescence two nearly opposite X-ray emitting poles. They are at a latitude between $\approx 44^\circ$ and $\approx 63^\circ$, tracing the asynchronous WD rotation ([Hellier 1997](#)). Consequently, the eclipse duration can vary depending on the relative position of the poles on the WD surface. For instance, at the start of a given eclipse, one pole could appear over the WD limb, while at the start of another eclipse it could be above the WD centre. In the first example, the eclipse would start sooner, producing a longer eclipse. However, the eclipse length variations are limited, considering that it takes the donor star between 22 and 35 s to travel the entire WD diameter ([Hellier 1997](#)), and the change in the relative position of the poles is a fraction of that distance. Furthermore, the eclipse duration reported by [Allan et al. \(1996\)](#) is the mean value obtained from the observation of six X-ray eclipses. While it would be ideal to obtain the duration from a very large number of X-ray eclipse observations with higher time resolution, we consider that the eclipse length in [Allan et al. \(1996\)](#) is accurate enough for our purposes. In fact, even if it were biased by ± 50 s, which is comparable to the length of the X-ray eclipse ingress/egress ([Kamata et al. 1991](#); [Hellier 1997](#); [Zengin Ćamurdan et al. 2018](#)), we would obtain an inclination $i = 80.2^\circ \pm 0.5^\circ$ for a 2000 ± 28 s eclipse duration and $i = 81.6^\circ \pm 0.5^\circ$ for 2100 ± 28 s. This change in the inclination would have a < 1 per cent effect on the dynamical masses, which illustrates the robustness of our results.

⁴ A fully consistent inclination is derived from the computation of a synthetic light curve considering the Roche lobe geometry and matching the eclipse duration. On the other hand, its analytical calculation under the approximation of a spherical donor with an effective Roche lobe radius (e.g. eq. 2 in [Dhillon et al. 1992](#)) gives $i = 79.6^\circ \pm 0.5^\circ$, that underestimates our numerically calculated value by 1.2° .

4 DISCUSSION

4.1 Stellar masses

The donor in XY Ari is consistent with a spectral type K6–M0 V. It has a mass $M_2 = 0.75 \pm 0.04 M_\odot$ and its Roche lobe volume radius can be calculated as $R_2 = \frac{P}{2\pi} \frac{v_{\text{rot}} \sin i}{\sin i} = 0.71 \pm 0.02 R_\odot$. The mass and radius are too high for a typical M0 V star, but they agree with the canonical mass and radius of a K6 V star, which are $\approx 0.7 M_\odot$ and $\approx 0.7 R_\odot$, respectively ([Pecaut & Mamajek 2013](#)). We also derive a surface gravity $\log g = 4.6 \pm 0.03$ dex. Based on these parameters, the donor star better fits a main sequence K6 star. Note that when we performed the spectral classification of the donor star (Section 3.2) we found that the best-matching IRTF template has an effective temperature of 4171 ± 39 K, which corresponds to a K6 V star according to [Pecaut & Mamajek \(2013\)](#).

[Zorotovic et al. \(2011\)](#) compiled all the WD masses from the literature that they considered as robust determinations⁵. Their sample contains 32 CVs with an average WD mass of $0.82 \pm 0.15 M_\odot$. [Pala et al. \(2022\)](#) considered the same criterion and updated the census to 54 CVs (see table 44 in the online supplementary material of their work). They also used high quality *Hubble Space Telescope* ultraviolet spectra and *Gaia* parallaxes to extend the sample to 89 systems, obtaining an average WD mass of $0.81^{+0.16}_{-0.20} M_\odot$. The WD in XY Ari is therefore more massive than the average at $> 2\sigma$. In fact, it would be among the three most massive WDs if included in the total sample of 89 CVs (now 90) from [Pala et al. \(2022\)](#). The other two systems are the dwarf novae U Gem ($M_1 = 1.20 \pm 0.05 M_\odot$) and IP Peg ($M_1 = 1.16 \pm 0.02 M_\odot$).

4.2 An updated estimate of the distance to XY Ari

Here we will exploit the constraint on the donor spectral classification and the photometry from the EMIR acquisition images to improve the distance estimate presented by [Littlefair et al. \(2001\)](#). From the multi-epoch target acquisitions we derive a phase-average magnitude of $K_s = 13.4 \pm 0.2$, while from the single acquisition done in the J -band we obtain $J = 16.4 \pm 0.2$. Using the ratio between the extinction in a given band and the colour excess, $A_\lambda/E(B-V)$, from ([Schlafly & Finkbeiner 2011](#)), we derive:

$$m_{K_s}^o - m_J^o = (M_{K_s} - M_J) - 0.407 \times E(B-V), \quad (7)$$

where m_λ^o and M_λ are the observed (reddened) apparent and absolute magnitudes of the donor star, respectively. Following [Littlefair et al. \(2001\)](#), we assume equal fractional light contribution f of the donor star to the total flux in the K_s - and J -bands. Thus, using a flat probability distribution for the spectroscopic constraint on f ($= 0.7 - 0.8$; Section 3.3) we derive $m_{K_s}^o = 13.7 \pm 0.2$ and $m_J^o = 16.7 \pm 0.2$. Adopting a K6 V donor star and employing the corresponding absolute magnitudes ($M_{K_s} = 4.56$, $M_J = 5.31$; [Pecaut & Mamajek 2013](#)), we obtain a colour excess $E(B-V) = 5.5 \pm 0.7$. From the colour excess we calculate the extinction in the K_s -band: $A_{K_s} = 0.302 \times E(B-V) = 1.7 \pm 0.2$ ([Schlafly & Finkbeiner 2011](#)). The intrinsic apparent magnitude of the likely K6 V donor star in XY Ari is $m_{K_s}^i = m_{K_s}^o - A_{K_s} = 12.0 \pm 0.3$. Using $m_{K_s}^i$ and M_{K_s} in

⁵ The methods considered as reliable by these authors are: analysis of eclipse light curves / radial velocity curves, derivation of the gravitational redshift from the systemic velocity of both the WD and the donor star, and modelling of the WD ultraviolet spectrum.

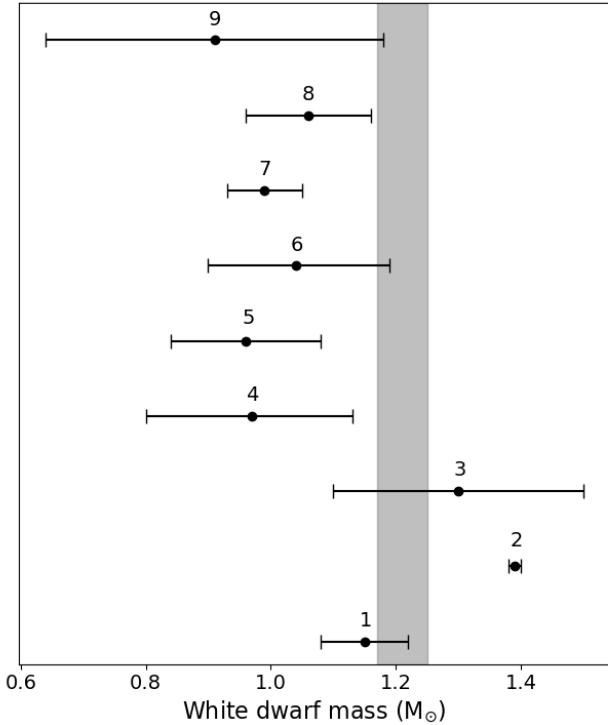


Figure 4. Comparison between the dynamical mass of the WD in XY Ari presented in this paper (shaded area, 1σ) and previous estimates obtained using spectral modelling of: *RXTE/ASCA/GINGA* soft X-ray data (labelled in the figure as 1, 2, and 3, respectively; Ramsay et al. 1998), *RXTE* soft X-ray data (4; Ramsay 2000), *Swift* hard X-ray data (5 and 8; Brunschweiler et al. 2009 and Suleimanov et al. 2019), *Suzaku* hard X-ray data (6; Yuasa et al. 2010) and *NuSTAR* hard X-ray data (7; Xu et al. 2019). An estimate based on the ratio of the iron emission lines in *NuSTAR* and *Suzaku* spectra is also included (9; Xu et al. 2019).

the distance modulus gives $d = 308 \pm 40$ pc. In comparison, a distance of 270 ± 100 pc was found by Littlefair et al. (2001) based on less-constrained parameters and characterization of the donor star.

4.3 Comparison with the WD mass from X-ray spectral modelling

In IPs, the temperature of the plasma in the region where the accreted material impacts the WD surface is thought to depend mainly on the WD mass and radius (Aizu 1973), which are linked through the theoretical mass-radius relation for WDs (Hamada & Salpeter 1961; Nauenberg 1972; Panei et al. 2000). The main cooling mechanism of the accreting region is assumed to be the emission of X-rays and, therefore, modelling of the X-ray spectrum can deliver an estimate of its WD mass (hereinafter M_1^X). Some authors have proposed that comptonization could be the main mechanism behind the X-ray emission in IPs (e.g. Maiolino et al. 2021), but the most extended and accepted models are based on thermal bremsstrahlung.

Ramsay et al. (1998) performed a multi-instrument X-ray study of XY Ari employing soft X-ray spectra and a multi-temperature bremsstrahlung model. They found instrument depending results in spite of the similar energy ranges. From 2 – 20 keV *RXTE/PCA* data they derived $M_1^X = 1.15 \pm 0.07 M_\odot$, while from 1 – 12 keV *ASCA* data (two or more detectors) the result was $M_1^X = 1.39 \pm 0.01 M_\odot$. Finally,

from 2 – 20 keV *Ginga/LAC* data the derived WD mass was $M_1^X = 1.3 \pm 0.2 M_\odot$. These measurements average to $M_1^X = 1.28 \pm 0.04 M_\odot$, which they deemed an overestimate since they expected a WD mass of $1 M_\odot$ based on assumptions such as a WD radius of $4.3 - 7.3 \times 10^8$ cm (Hellier 1997) and $M_2 = 0.62 M_\odot$ (from Patterson’s mass-radius relation, Patterson 1984). Our dynamical study reveals that, in fact, their mean M_1^X agrees within 1σ of our WD mass. However, it should be noted that this average X-ray value comes from inconsistent estimates. Later, Ramsay (2000) used a refined version of the previous model to fit 2 – 20 keV *RXTE/PCA* spectra of several IPs. For XY Ari, this improved model yielded $M_1^X = 0.97^{+0.16}_{-0.17} M_\odot$, which only agrees at the 2σ level with our dynamical measurement. In general, soft (< 20 keV) X-ray spectra do not provide accurate estimates for WD masses in IPs, since for masses $> 0.6 M_\odot$ the maximum post-shock temperature is > 20 keV (Suleimanov et al. 2005). Further, the soft spectrum of many IPs is strongly affected by absorption and reflection components that are still not well understood (Suleimanov et al. 2019).

WD mass estimates for XY Ari have also been derived from hard (> 20 keV) X-ray data. Brunschweiler et al. (2009) presented a fit to a 15 – 195 keV *Swift/BAT* spectrum of XY Ari employing the multi-temperature bremsstrahlung model of Suleimanov et al. (2005) and obtained $M_1^X = 0.96 \pm 0.12 M_\odot$. Likewise, Yuasa et al. (2010) used an improved version of the previous model with 3 – 50 keV *Suzaku* data and found $M_1^X = 1.04^{+0.15}_{-0.14} M_\odot$. Following a similar approach, Xu et al. (2019) modelled a 3 – 50 keV *NuSTAR* spectrum and derived $M_1^X = 0.99 \pm 0.06 M_\odot$. Finally, Suleimanov et al. (2019) employed a more complex model that considers a finite fall height for the accreted matter. From *Swift/BAT* XY Ari data they obtained $M_1^X = 1.06 \pm 0.10 M_\odot$, which is below the dynamical WD mass, but is very close to a 1σ level agreement. These comparisons show that the M_1^X values derived from hard X-ray spectral bands (which are supposed to be more reliable) may well underestimate the mass of the WD in XY Ari. In this respect, Álvarez-Hernández et al. (2021) found that most of the estimates with uncertainties $< 0.2 M_\odot$ obtained from X-ray spectral fitting for the WD mass in the IP GK Per (dynamical mass $M_1 \approx 1 M_\odot$) are underestimates, while different indirect techniques such as deriving the quiescence-to-outburst Alfvén radius ratio from X-ray spectra or modelling the nova event optical light curve, provided accurate values.

Other methods have been explored to derive WD masses in IPs using X-ray data. In particular, Ezuka & Ishida (1999) used a 5 – 10 keV *ASCA* spectrum of XY Ari to derive a temperature of $4.9^{+9.9}_{-4.9}$ keV from the intensity ratio of the 6.7 and 7.0 keV iron emission lines and theoretical relations from Mewe et al. (1985). They also fitted the continuum, obtaining 16^{+21}_{-6} keV. Similar temperature differences appeared for most magnetic CVs in their study, as a consequence of the temperature gradient in the plasma. The continuum temperature was expected to represent an average of the temperature distribution, so they derived a relation between both temperature determinations and used it to derive the WD masses from the iron emission line ratios. Unfortunately, they did not provide a value for XY Ari. We guess the reasons for that were poorly resolved emission lines and that XY Ari clearly deviates from the relation between temperature determinations (see the position of XY Ari in their fig. 4). More recently, Xu et al. (2019) derived a relation between WD masses in IPs and the intensity ratio of the 6.7 and 7.0 keV iron emission lines based on synthetic (model-generated) spectra. They derived $M_1^X = 0.91 \pm 0.27 M_\odot$ for XY Ari, whose uncertainty is too high to draw any conclusion.

In brief, a number of the M_1^X values reported are not in good agreement with our dynamical WD mass. Figure 4 gives a visual

Table 5. Fundamental parameters of XY Ari presented in this article.

K_2 (km s ⁻¹)	256 ± 2
$v_{\text{rot}} \sin i$ (km s ⁻¹)	141 ± 3
q	0.62 ± 0.02
i (°)	80.8 ± 0.5
M_1 (M _⊙)	1.21 ± 0.04
M_2 (M _⊙)	0.75 ± 0.04
R_2 (R _⊙)	0.71 ± 0.02
d (pc)	308 ± 40

summary of the contents of this section. In view of our results and those presented in [Álvarez-Hernández et al. \(2021\)](#) for GK Per, we warn that WD average masses in IPs obtained from X-ray spectral modelling should be taken with caution. The improvement of hard X-ray spectrometers and refined accretion models have allowed to reduce very significantly the statistical uncertainties in the M_1^X values (e.g. [Shaw et al. 2020](#)), but there still exist important systematic deviations that must be addressed. In this regard, [Belloni et al. \(2021\)](#) suggested that X-ray spectral modelling alone may not be enough to derive reliable physical parameters. They showed that there is a degeneracy in the parameter space of X-ray spectral models. Multiple combinations of the parameters (WD mass, magnetic field strength, magnetospheric radius and specific accretion rate) can produce the same spectrum. According to these authors, additional data, such as simultaneous X-ray light curves, are required to break the degeneracy and obtain accurate estimates of the parameters.

5 CONCLUSIONS

We have performed a dynamical study of the eclipsing IP XY Ari using GTC/EMIR NIR spectra taken in 2018 – 2022. We constrain the spectral type of the donor star, derive its radial velocity curve and measure its rotational broadening. We found that the donor star is consistent with a K6 V star with $K_2 = 256 \pm 2$ km s⁻¹ and $v_{\text{rot}} \sin i = 141 \pm 3$ km s⁻¹. Using these values we derived the binary mass ratio $q = 0.62 \pm 0.02$, which allowed us to better constrain the orbital inclination, $i = 80.8^\circ \pm 0.5^\circ$. We finally derive the dynamical masses $M_1 = 1.21 \pm 0.04 M_\odot$ for the WD and $M_2 = 0.75 \pm 0.04 M_\odot$ for the donor star. The WD is at least the third most massive ever found in a CV. Table 5 compiles all the fundamental parameters of XY Ari presented in this work.

We compared our dynamical WD mass with estimates from X-ray spectral modelling values and found disagreement. Specifically, we observe that even recent models applied to hard X-ray (> 20 keV) data may underestimate the WD mass. We also made a comparison with estimates from X-ray iron emission-line ratios, but were unable to find any clear trend due to the large uncertainties reported and the inconsistency between the works that have used this method.

The present work is another piece of evidence that WD masses from current X-ray methods may suffer from significant systematic deviations. Further testing of these techniques requires precise WD mass determinations in X-ray bright IPs. More accurate dynamical studies would serve very well to this purpose.

ACKNOWLEDGEMENTS

We thank the anonymous referee for insightful comments and constructive suggestions. We are thankful to the GTC staff, in particular Antonio L. Cabrera Lavers, for their help and assistance in obtaining the spectroscopy presented in this paper. We thank Alina Streblyanska for sharing her expertise in EMIR with us. We also thank Nicolás Cardiel López for clarifying us some aspects about PYEMIR. This work was supported by the Agencia Estatal de Investigación del Ministerio de Ciencia e Innovación (MCIN/AEI) and the European Regional Development Fund (ERDF) under grants AYA2017–83216–P, AYA2017–83383–P and PID2021–124879NB–I00. MAPT was also supported by a Ramón y Cajal Fellowship RYC–2015–17854. PR-G acknowledges support from the Consejería de Economía, Conocimiento y Empleo del Gobierno de Canarias and the European Regional Development Fund (ERDF) under grant with reference ProID2021010132. The use of the MOLLY package developed by Tom Marsh is acknowledged.

DATA AVAILABILITY

The data used in this article are publicly available at the 10.4-m Gran Telescopio Canarias archive (<https://gtc.sdc.cab.inta-csic.es/gtc/>) under program ids GTC76-17B, GTC152-18B, GTC108-20B and GTCMULTIPLE2E-21A.

REFERENCES

- Aizu K., 1973, *Progress of Theoretical Physics*, 49, 1184
 Alam S., et al., 2015, *ApJS*, 219, 12
 Allan A., Hellier C., Ramseyer T. F., 1996, *MNRAS*, 282, 699
 Álvarez-Hernández A., et al., 2021, *MNRAS*, 507, 5805
 Arentsen A., et al., 2019, *A&A*, 627, A138
 Belloni D., et al., 2021, *ApJS*, 256, 45
 Billington I., Marsh T. R., Dhillon V. S., 1996, *MNRAS*, 278, 673
 Brunschweiler J., Greiner J., Ajello M., Osborne J., 2009, *A&A*, 496, 121
 Cardiel N., et al., 2019, in Teuben P. J., Pound M. W., Thomas B. A., Warner E. M., eds, *Astronomical Society of the Pacific Conference Series Vol. 523, Astronomical Data Analysis Software and Systems XXVII*. p. 317
 Chambers K. C., et al., 2016, arXiv e-prints, p. arXiv:1612.05560
 Chanan G. A., Middleditch J., Nelson J. E., 1976, *ApJ*, 208, 512
 Chubak C., Marcy G., 2011, in *American Astronomical Society Meeting Abstracts #217*. p. 434.12
 Claret A., Díaz-Cordoves J., Gimenez A., 1995, *A&AS*, 114, 247
 Cutri R. M., et al., 2003, *VizieR Online Data Catalog*, p. II/246
 Davey S., Smith R. C., 1992, *MNRAS*, 257, 476
 Dhillon V. S., Jones D. H. P., Marsh T. R., Smith R. C., 1992, *MNRAS*, 258, 225
 Eggleton P. P., 1983, *ApJ*, 268, 368
 Ezuka H., Ishida M., 1999, *ApJS*, 120, 277
 Fouqué P., et al., 2018, *MNRAS*, 475, 1960
 Garzón F., EMIR Team 2016, in Skillen I., Balcells M., Trager S., eds, *Astronomical Society of the Pacific Conference Series Vol. 507, Multi-Object Spectroscopy in the Next Decade: Big Questions, Large Surveys, and Wide Fields*. p. 297
 Garzón F., et al., 2022, arXiv e-prints, p. arXiv:2209.15395
 Gonneau A., et al., 2020, *A&A*, 634, A133
 Gray D. F., 1992, *The Observation and Analysis of Stellar Photospheres*. Cambridge University Press, Cambridge
 Halpern J. P., Patterson J., 1987, *ApJ*, 312, L31
 Hamada T., Salpeter E. E., 1961, *ApJ*, 134, 683
 Hellier C., 1997, *MNRAS*, 291, 71
 Hellier C., Mukai K., Beardmore A. P., 1997, *MNRAS*, 292, 397

- Hessman F. V., Robinson E. L., Nather R. E., Zhang E. H., 1984, *ApJ*, **286**, 747
- Houdebine É. R., Mullan D. J., Doyle J. G., de La Vieuville G., Butler C. J., Paletou F., 2019, *AJ*, **158**, 56
- Kamata Y., Tawara Y., Koyama K., 1991, *ApJ*, **379**, L65
- Koyama K., et al., 1991, *ApJ*, **377**, 240
- Kraft R. P., 1964, *ApJ*, **139**, 457
- Littlefair S. P., Dhillon V. S., Marsh T. R., 2001, *MNRAS*, **327**, 669
- Luck R. E., 2015, *AJ*, **150**, 88
- Luck R. E., 2017, *AJ*, **153**, 21
- Luyten W. J., 1936, *ApJ*, **84**, 85
- Maiolino T., Titarchuk L., Wang W., Frontera F., Orlandini M., 2021, *ApJ*, **911**, 80
- Marsh T. R., 1988, *MNRAS*, **231**, 1117
- Marsh T. R., Robinson E. L., Wood J. H., 1994, *MNRAS*, **266**, 137
- Martin J. S., Jones D. H. P., Smith R. C., 1987, *MNRAS*, **224**, 1031
- Martin J. S., Friend M. T., Smith R. C., Jones D. H. P., 1989, *MNRAS*, **240**, 519
- Mateo M., Szkody P., Garnavich P., 1991, *ApJ*, **370**, 370
- Mewe R., Gronenschild E. H. B. M., van den Oord G. H. J., 1985, *A&AS*, **62**, 197
- Nauenberg M., 1972, *ApJ*, **175**, 417
- Niedzielski A., Deka-Szymankiewicz B., Adamczyk M., Adamów M., Nowak G., Wolszczan A., 2016, *A&A*, **585**, A73
- Pala A. F., et al., 2022, *MNRAS*, **510**, 6110
- Panei J. A., Althaus L. G., Benvenuto O. G., 2000, *A&A*, **353**, 970
- Patterson J., 1984, *ApJS*, **54**, 443
- Patterson J., Halpern J. P., 1990, *ApJ*, **361**, 173
- Pecaut M. J., Mamajek E. E., 2013, *ApJS*, **208**, 9
- Ramsay G., 2000, *MNRAS*, **314**, 403
- Ramsay G., Cropper M., Hellier C., Wu K., 1998, *MNRAS*, **297**, 1269
- Rayner J. T., Cushing M. C., Vacca W. D., 2009, *ApJS*, **185**, 289
- Rojas-Ayala B., Covey K. R., Muirhead P. S., Lloyd J. P., 2012, *ApJ*, **748**, 93
- Schlafly E. F., Finkbeiner D. P., 2011, *ApJ*, **737**, 103
- Shaw A. W., et al., 2020, *MNRAS*, **498**, 3457
- Smette A., et al., 2015, *A&A*, **576**, A77
- Soubiran C., et al., 2018, *A&A*, **616**, A7
- Sousa S. G., Santos N. C., Israelian G., Mayor M., Udry S., 2011, *A&A*, **533**, A141
- Southwell K. A., Still M. D., Smith R. C., Martin J. S., 1995, *A&A*, **302**, 90
- Steehgs D., Jonker P. G., 2007, *ApJ*, **669**, L85
- Suleimanov V., Revnivtsev M., Ritter H., 2005, *A&A*, **435**, 191
- Suleimanov V. F., Doroshenko V., Werner K., 2019, *MNRAS*, **482**, 3622
- Takano S., et al., 1989, *IAU Circ.*, **4745**, 1
- Torres M. A. P., Casares J., Martínez-Pais I. G., Charles P. A., 2002, *MNRAS*, **334**, 233
- Torres M. A. P., Casares J., Jiménez-Ibarra F., Álvarez-Hernández A., Muñoz-Darias T., Armas Padilla M., Jonker P. G., Heida M., 2020, *ApJ*, **893**, L37
- Vacca W. D., Cushing M. C., Rayner J. T., 2003, *PASP*, **115**, 389
- Wade R. A., Horne K., 1988, *ApJ*, **324**, 411
- Warner B., 1995, *Cambridge Astrophysics Series*, **28**
- Xu X.-j., Yu Z.-l., Li X.-d., 2019, *ApJ*, **878**, 53
- Yee S. W., Petigura E. A., von Braun K., 2017, *ApJ*, **836**, 77
- Yuasa T., Nakazawa K., Makishima K., Saitou K., Ishida M., Ebisawa K., Mori H., Yamada S., 2010, *A&A*, **520**, A25
- Zengin Çamurdan D., Balman Ş., Burwitz V., 2018, *MNRAS*, **477**, 4035
- Zorotovic M., Schreiber M. R., Gänsicke B. T., 2011, *A&A*, **536**, A42
- Zuckerman B., Becklin E. E., McLean I. S., Patterson J., 1992, *ApJ*, **400**, 665

This paper has been typeset from a $\text{\TeX}/\text{\LaTeX}$ file prepared by the author.